Chinese Chemical Letters 36 (2025) 110073

Contents lists available at ScienceDirect

Chinese Chemical Letters

journal homepage: www.elsevier.com/locate/cclet

Highly efficient green light-excited AIE photosensitizers derived from BF_2-curcuminoid for specific photodynamic eradication of Gram-negative bacteria

Ziyong Li[a,1], Jinzhao Song[a,1], Xinyu Gao[a], Xiaoxie Ma[b], Keyu Liu[a], Ziwei Ma[a], Qilian Wang[a], Xinliang Zeng[a], Haining Zhang[a], Pei Zhang[a], Hui Guo[a,*], Jun Yin[b,*]

[a] Luoyang Key Laboratory of Organic Functional Molecules, College of Food and Drug, College of Chemistry and Chemical Engineering, Department of Life Science, Luoyang Normal University, Luoyang 471934, China
[b] State Key Laboratory of Green Pesticide, International Joint Research Center for Intelligent Biosensor Technology and Health, College of chemistry, Central China Normal University, Wuhan 430079, China

ARTICLE INFO

Article history:
Received 13 March 2024
Revised 28 May 2024
Accepted 30 May 2024
Available online 31 May 2024

Keywords:
Photodynamic therapy (PDT)
Photosensitizers
Curcuminoid
Aggregation-induced emission (AIE)
Gram-negative bacteria

ABSTRACT

Diseases associated with bacterial infection, especially those caused by gram-negative bacteria, have been posing a serious threat to human health. Photodynamic therapy based on aggregation-induced emission (AIE) photosensitizer have recently emerged and provided a promising approach for bacterial discrimination and efficient photodynamic antimicrobial applications. However, they often suffer from the shorter excitation wavelength and lower molar extinction coefficients in the visible region, severely limiting their further applications. Herein, three novel BF_2-curcuminoid-based AIE photosensitizers, **TBBC**, **TBC** and **TBBC-C8**, have been rationally designed and successfully developed, in which OCH_3- and OC_8H_{17}-substituted tetraphenylethene (TPE) groups serve as both electron donor (D) and AIE active moieties, BF_2bdk group functions as electron acceptor (A), and styrene (or ethylene) group as π-bridge in this D-π-A-π-D system, respectively. As expected, these resulting BF_2-curcuminoids presented solvent-dependent photophysical properties with large molar extinction coefficients in solutions and excellent AIE properties. Notably, **TBBC** showed an effective singlet oxygen generation efficiency thanks to the smaller singlet-triplet energy gap (ΔE_{ST}), and remarkable photostability under green light exposure at 530 nm (8.9 mW/cm^2). More importantly, **TBBC** was demonstrated effectiveness in selective staining and photodynamic killing of *Escherichia coli* (*E. coli*) *in vitro* probably due to its optimal molecular size compared with **TBC** and **TBBC-C8**. Therefore, **TBBC** will have great potential as a novel AIE photosensitizer to apply in the discrimination and selective sterilization between Gram-positive and Gram-negative bacteria.

The traditional antibiotic medications for bacterial infections have confronted increasing challenges with the emergence and widespread of multidrug-resistant bacteria, posing a serious threat to global human health and led to millions of deaths worldwide [1–5]. In particular, infectious caused by Gram-negative (G(−)) bacteria are extremely difficult to treat compared to Gram-positive (G(+)) bacterial infection resulted from their natural outer membrane, highly selective porins, and abundant efflux pumps, which confers intrinsically resistance to G(−) bacteria to many antibiotics or other antibacterial materials [6]. Therefore, this poses a serious challenge to the existing antibiotics and an urgent need to develop new antibiotics to defend against G(−) bacteria-associated infections. However, the development of new antibiotics has far behind the outbreak of antibiotic-resistant bacteria. Thus, it is of great significance to explore novel antibacterial strategies to cope with antibiotic resistance. Among them, photodynamic therapy (PDT) provides a promising bactericidal approach that is not prone to resistance, which employs the photosensitizer (PS) to generate reactive oxygen species (ROS), especially singlet oxygen ($^1O_2$), upon exposure to light at specific wavelength [7–9]. As the most important component in PDT, a large number of PSs have been extensively exploited and applied in recent years. Nevertheless, most of these PSs suffer from insufficient $^1O_2$ generation and fluorescence quenching in the aggregated state or a hydrophilic physiological environment, which severely limits their applications in the imaging-guided PDT. In this context, PSs with aggregation-

* Corresponding authors.
E-mail addresses: guohui@lynu.edu.cn (H. Guo), yinj@ccnu.edu.cn (J. Yin).
[1] These authors contributed equally to this work.

https://doi.org/10.1016/j.cclet.2024.110073
1001-8417/

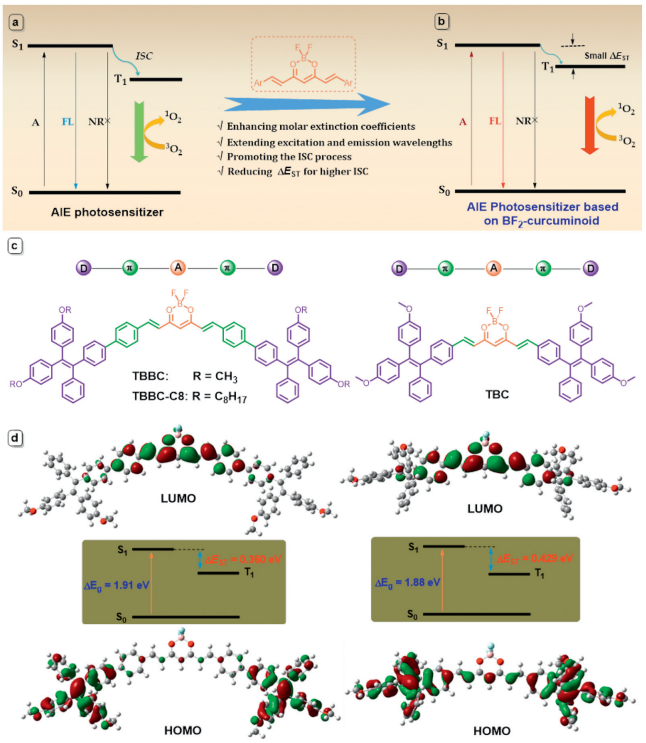

Fig. 1. (a) Simplified Jablonski diagram of singlet oxygen generation for AIE photosensitizer. (b) Simplified Jablonski diagram of singlet oxygen generation for AIE photosensitizer based on BF_2-curcuminoid. (c) Chemical structures of AIE photosensitizer based on BF_2-curcuminoid (**TBBC**, **TBC** and **TBBC-C8**). (d) The calculated spatial distributions of HOMO and LUMO of **TBBC** (left) and **TBC** (right). A: absorption, NR: nonradiative decay, FL: fluorescence, S_0: ground state, S_1: excited singlet state, T_1: excited triplet state, $^3O_2$: normal oxygen, $^1O_2$: singlet oxygen, ISC: intersystem crossing.

induced emission (AIE) features have been recently emerged [10–15]. As expected, these AIE PSs showed strong fluorescence and efficient $^1O_2$ generation in the aggregated state owing to the minimized nonradiative decay (NR) *via* restriction of intramolecular motion (Fig. 1a). However, the lower molar extinction coefficients in the visible region and the shorter excitation wavelength for most AIE PSs still need to be addressed for their further applications because they have the narrow light-harvesting ability.

Fortunately, a class of highly luminescent organoboron complexes with large molar extinction coefficients, *i.e.*, difluoroboron β-diketonate (BF_2bdk) complexes [16,17], may provide a possible solution to the above issues. Recently, the BF_2bdk complexes have shown extensive applications in bioimaging, organic electronics, and photovoltaics due to their rich photophysical properties. However, a common limitation of these complexes is their tendency to exhibit shorter absorption and emission wavelengths, constraining their broader application. To address this, researchers have explored the integration of BF_2 into curcumin analogues, creating BF_2-curcuminoid complexes. This modification not only shifts the absorption and emission wavelengths towards the red end of the spectrum but also increases molecular rigidity and enhances photostability. BF_2-curcuminoid complexes have been utilized in various technologies, including near-infrared (NIR) fluorescent probes [18–23], photoacoustic imaging [24–28], NIR thermally activated delayed fluorescence (TADF) photosensitizers [29], TADF switches [30], and NIR TADF organic light-emitting diodes (OLEDs) [31,32]. This innovation in BF_2-curcuminoid design is particularly inspiring in the context of AIE PSs. By incorporating the strong electron-withdrawing BF_2bdk group into tetraphenylethene (TPE)-type AIE PSs, it is anticipated that this approach will yield novel AIE PSs that are excited by longer wavelength visible light and possess large molar extinction coefficients. Additionally, this strategy is expected to endow BF_2-curcuminoid complexes with unique AIE characteristics, enhancing their potential for broader applications.

To validate this hypothesis, we have rationally designed and prepared two BF_2-curcuminoid-based AIE PSs (**TBBC** and **TBC**) (Figs. 1b and c), in which methoxy-substituted TPE (MTPE) groups serve as both electron donor (D) and AIE active moieties, BF_2bdk group functions as electron acceptor (A), and styrene (or ethylene) group as π-bridge in this D-π-A-π-D system, respectively. For contrast, the bulky C8 alkyl chains-substituted analogue (**TBBC-C8**) was also designed and synthesized to verify the speculation about the mechanism of admirable antibacterial action towards *E. coli*. As expected, the as-prepared **TBBC**, **TBC** and **TBBC-C8** presented solvent-dependent photophysical properties with large molar extinction coefficients in solutions, and excellent AIE properties in mixtures of toluene/DMSO. Remarkably, **TBBC** was particularly effective in generating singlet oxygen ($^1O_2$) when exposed to green light at 530 nm. It also showed a notable capability for selective staining and photodynamic inactivation of *E. coli*, indicating its potential as an innovative antibacterial PDT agent in the fight against drug-resistant bacterial infections.

In such photosensitive system, the molecular design principles for incorporating BF_2bdk group into the AIE PSs are primarily focused on the following aspects (Fig. 1): (I) Enhancing molar extinction coefficients in favor of light-harvesting ability of AIE PSs; (II) Extending excitation wavelength to achieve long wavelength visible light excitation of AIE PSs; (III) Promoting the intersystem crossing (ISC) because active nonbonding p electrons on the BF_2bdk group are devoted to enhancing the spin-orbital coupling (SOC); (IV) Separating the highest occupied molecular orbital (HOMO)-lowest unoccupied molecular orbital (LUMO) distribution to reduce ΔE_{ST} ($E_{S1} - E_{T1}$) for higher ISC [33], which is achieved by inserting a benzene ring between the donor and acceptor for **TBBC** to fine-tune their distance and torsional angle compared to the analogue **TBC**. As shown in Fig. 1d, the HOMO distribution of **TBBC** is positioned at two MTPE groups and LUMO is mainly fixed at central BF_2-curcuminoid skeleton. This indicates an efficient separation of HOMO and LUMO, thus resulting in a small ΔE_{ST} value (0.360 eV). For contrast, another AIE PS (**TBC**) without benzene ring bridging is designed and synthesized, which shows a much bigger ΔE_{ST} (0.429 eV) compared to **TBBC** resulting from its partially overlapped HOMO and LUMO (Fig. 1d and Table S1 in Supporting information). In addition, the bulky C8-substituted analogue (**TBBC-C8**) of **TBBC** is also obtained to verify the speculation about the mechanism of admirable antibacterial action towards *E. coli*. Unsurprisingly, no appreciable differences in the HOMO and LUMO orbital distribution and its ΔE_{ST} (0.349 eV) for **TBBC-C8** are observed compared with **TBBC** (Fig. S1 and Table S1 in Supporting information), further implying that the incorporation of C8 alkyl chain may have insignificant influence on the generation of singlet oxygen. As depicted in Scheme S1 (Supporting information), **TBBC** and **TBC** were prepared by the Knoevenagel condensation reaction between MTPE-CHO (**2** or **3**) and BF_2 complex of pentane-2,4-dione (**4**) using *n*-$BuNH_2$ as the catalysis in anhydrous toluene in the yield of 48% and 57%, respectively. A similar approach was used to synthesize **TBBC-C8** in the yield of 36%. Their chemical structures were well characterized by ^{1}H NMR, ^{13}C NMR and high-resolution mass spectrometry (HRMS) (Figs. S25–S39 in Supporting information). From ^{1}H NMR spectrum of **TBBC**, the coupling constants of double bonds were *ca.* 15.5 Hz, suggesting a stable *trans*-configuration for both ethylene bonds in **TBBC**.

With these curcuminoid-BF_2 complexes in hand, their photophysical properties were investigated in solvents with different polarity. As depicted in Fig. 2a and Table S2 (Supporting information), **TBBC** clearly showed a maximum absorption band rang-

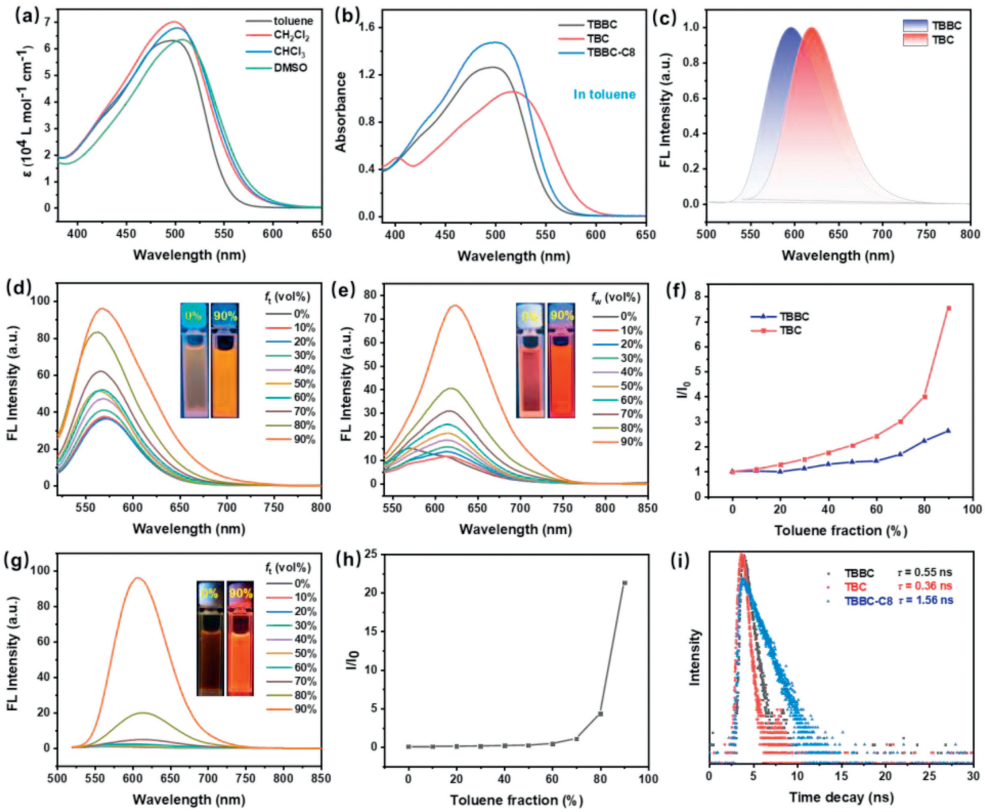

Fig. 2. (a) The UV–vis absorption spectra of **TBBC** in different solvents (2.0×10^{-5} mol/L). (b) The UV–vis absorption spectra of **TBBC**, **TBC** and **TBBC-C8** in toluene (2.0×10^{-5} mol/L). (c) The fluorescence spectra of **TBBC** and **TBC** in toluene (2.0×10^{-5} mol/L) ($\lambda_{ex} = 498$ nm and 517 nm, respectively). (d, e) The fluorescence spectra of **TBBC** (d) and **TBC** (e) in different mixtures of toluene/DMSO (v/v) (2.0×10^{-5} mol/L) ($\lambda_{ex} = 500$ nm and 520 nm, respectively). Insert: their corresponding photographs in 0% and 90% toluene solutions under 365 nm UV light. (f) The dependence of the emission intensity on the toluene fraction (f_t). (g) The fluorescence spectra of **TBBC-C8** in different mixtures of toluene/THF (v/v) (2.0×10^{-5} mol/L) ($\lambda_{ex} = 500$ nm). Insert: their corresponding photographs in 0% and 90% toluene solutions under 365 nm UV light. (h) The dependence of the emission intensity on the toluene fraction (f_t). (i) Time-resolved decay profiles of **TBBC**, **TBC** and **TBBC-C8** in the aggregated state.

ing from 498 nm to 508 nm in four various solvents, which is attributable to intramolecular charge transfer (ICT) transition from TPE groups to the central difluoroboron β-diketonate moiety [34]. The perceptible redshift was observed with increasing solvent polarity. More importantly, **TBBC** showed high extinction coefficients ($\varepsilon = 6.31 \times 10^4$–$7.02 \times 10^4$ L mol^{-1} cm^{-1}) in the visible region, which indicates the outstanding visible light-harvesting capability for **TBBC**. Compared with **TBBC**, the maximum absorption wavelength of **TBC** revealed an obvious redshift ($\Delta\lambda = ca.$ 20 nm) in the same solvent (Figs. S2, S4–S6 and Table S2 in Supporting information), which is attributed to increased π-conjugation for **TBC** without the benzene ring acting as a bridge linker. As expected, **TBBC-C8** bearing four alkyl chains displayed negligible changes in ultraviolet (UV) absorption because alkyl chains have no obvious effect on the conjugated system (Figs. S3–S6 and Table S2 in Supporting information). As illustrated in Fig. 2c, Figs. S7–S9 and Table S2 (Supporting information), **TBBC** presented an intense orange fluorescence with high fluorescence quantum yield ($\Phi_F = 0.23$) in weak polar toluene (poor solvent), while relatively inefficient emission with lower Φ_F (from 0.06 to 0.008) was detected in the larger polar solvents (good solvents: CH_2Cl_2, $CHCl_3$ and DMSO). Comparatively speaking, **TBC** emitted a strong red fluorescence and showed red-shifted changes ($\Delta\lambda_{em} = 24$–51 nm) in fluorescence emission in solvents with different polarity (Table S2). In addition, **TBBC-C8** exhibited a similar fluorescence performance to **TBBC** under the same conditions (Fig. S10 and Table S2 in Supporting information).

Whereafter, their AIE performance was evaluated in the mixed solvents (toluene/DMSO). As depicted in Figs. 2d and f, **TBBC** showed a weak emission in pure DMSO. As toluene fraction (f_t) increased from 0% to 20%, negligible fluorescence change was detected. When f_t was greater than 20%, the emission peak at 562 nm ($f_w = 30\%$) was gradually red-shifted to 570 nm ($f_t = 90\%$), and its emission intensity significantly increased and reached the maximum value at $f_w = 90\%$ due to the formation of the aggregates, which was accompanied by the appearance of an intense orange fluorescence (insert in Fig. 2d). Furthermore, a much higher quantum yield ($\Phi_f = 0.19$) for **TBBC** was obtained in 90% water mixed solutions compared with that in pure DMSO ($\Phi_f = 0.008$), as well as fluorescence lifetimes ranging from 0 ns to 0.55 ns (Fig. 2i). Moreover, similar AIE properties for **TBC** ($\lambda_{em} = 624$ nm, $\Phi_f = 0.27$, $\tau = 0.36$ ns) and **TBBC-C8** ($\lambda_{em} = 608$ nm, $\Phi_f = 0.30$, $\tau = 1.56$ ns) were observed with the increase of f_t from 0% to 90% (Figs. 2e–i and Fig. S11 in Supporting information). Therefore, these results clearly implied that the incorporation of curcuminoid-BF_2 did not affect the AIE characteristics of OCH_3- and OC_8H_{17}-substituted TPE moieties.

In consideration of their excellent luminescent properties in the aggregated state, the bacteria imaging capabilities for these BF_2-curcuminoids were further explored. Firstly, the hydrophobic **TBBC** was made into water-soluble nanoparticles (abbreviated as **TBBC** NPs) by encapsulation of the amphiphilic Pluronic F-127, as illustrated in Fig. 3a. The dynamic light scattering (DLS) experiment showed that the average hydrodynamic diameter of the resulting nanoparticles (**TBBC** NPs) was determined to be *ca.* 109 nm (Fig. 3c), which favors efficient accumulation at the bacterial sites for fluorescence imaging and antibacterial PDT. Subsequently, **TBC** NPs (average size = 83 nm) and **TBBC-C8** NPs (average size = 122 nm) were also successfully fabricated through the same bottom-up approach using F-127 as the doping matrix (Figs. S12 and S13 in Supporting information).

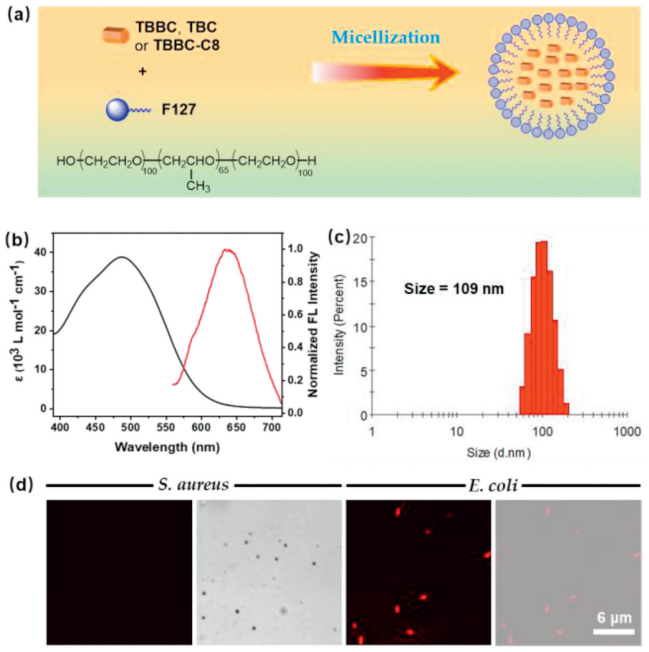

Fig. 3. (a) Schematic representation of the preparation of the nanoparticles by using an amphiphilic Pluronic F-127 as the doping matrix (**TBBC** NPs, **TBC** NPs and **TBBC-C8** NPs). (b) The absorption and emission spectra of **TBBC** NPs in water (2.0×10^{-5} mol/L, $\lambda_{ex} = 488$ nm). (c) DLS profiles of **TBBC** NPs. (d) Fluorescence and merged images of bacteria (*S. aureus* and *E. coli*) incubated with **TBBC** NPs for 20 min.

The shape and size of these prepared nanoparticles were confirmed by transmission electron microscopy (TEM), manifesting uniform spheres with the different size for **TBC** NPs, **TBBC** NPs, and **TBBC-C8** NPs (Fig. S14 in Supporting information). More importantly, the as-prepared **TBBC** NPs displayed a broad visible light absorption ranging from 390 nm to 675 nm (Fig. 3b). The aqueous suspension of **TBBC** NPs emitted a bright red fluorescence ($\lambda_{em} = 640$ nm, $\Phi_f = 0.08$) under irradiation with 365 nm UV light (Fig. 3b and Table S2), which is beneficial for fluorescence imaging in biomedical fields. In comparison, **TBC** NPs showed a red-shifted fluorescence emission ($\lambda_{em} = 668$ nm, $\Phi_f = 0.05$) in aqueous solution (Fig. S15 and Table S2 in Supporting information) due to the extended conjugated system compared with **TBBC**. Besides, **TBBC-C8** NPs exhibited a similar maximum emission wavelength at 642 nm in water, as well as a stronger red fluorescence emission than **TBBC** NPs (Fig. S16 and Table S2 in Supporting information), suggesting incorporation of C8 alkyl chains can prevent the intermolecular stacking to enhance the AIE effect.

Encouraged by the remarkable AIE performance and red emission in nanoaqueous solution, we selected Gram-positive *S. aureus* and Gram-negative *E. coli* as representatives to preliminarily assess the bacteria staining capabilities of these BF_2-curcuminoids. As depicted in Fig. 3d, when two kinds of bacteria were incubated with **TBBC** NPs, almost no fluorescence signal was detected for *S. aureus*, while the distinct fluorescence signal was accidentally visualized in *E. coli*. To the best of our knowledge, most previously reported AIE photosensitizer molecules exhibited selective imaging for Gram-positive bacteria through hydrophobic and electrostatic interactions [35–38], which is attributable to the distinctive multilayer outer membrane structures possessed by Gram-negative bacteria [39]. Additionally, the poring channels in the outer envelope of Gram-negative bacteria can expel small dye molecules. Therefore, the experimental result that **TBBC** NPs displayed a selective bacteria imaging for Gram-negative *E. coli* was very surprising to us. However, when both *S. aureus* and *E. coli* were incubated with **TBC** NPs and **TBBC-C8** NPs under the same conditions, no fluorescence signals were detected in neither *S. aureus* nor *E. coli*, which may be attributed to the fact that the smaller **TBC** and larger **TBBC-C8** do not readily bind to the bacterial cell membrane. Consequently, these bacterial staining results implied that **TBBC** as a novel AIE fluorescent dyes has great potential for application in discriminating between Gram-positive and Gram-negative bacteria.

To speculate on the reason for the differences in their ability to target *S. aureus* and *E. coli*, zeta potentials (ζ) usually reflecting the electrical charge on the bacterial surface were subsequently determined to investigate interactions between the bacteria and these BF_2-curcuminoids. As illustrated in Fig. S17 (Supporting information), after *S. aureus* was incubated with **TBBC**, **TBC** and **TBBC-C8**, the corresponding ζ potentials of *S. aureus* exhibited an obvious negative shift in contrast with that of *S. aureus* alone, which implies no electrostatic interactions between these BF_2-curcuminoids and the negatively charged bacterial surface. Thus, no fluorescence signals for **TBBC**, **TBC** and **TBBC-C8** were detected in *S. aureus*. Moreover, an apparent positive shift ($\Delta\zeta = 4.44$ eV) for the ζ potential of *E. coli* when incubated with **TBBC** compared with that of *E. coli* alone, which can be attributed to the electrostatic interactions between the negatively charged bacterial surface and the AIE PS **TBBC**, thus leading to neutralization of the negative charge on the surface of *E. coli*. However, the ζ potentials of *E. coli* displayed a negligible change after incubated with smaller **TBC** and larger **TBBC-C8** with C8 alkyl chains compared to *E. coli* alone. This may be because **TBC** can effectively insert into the outer membrane on *E. coli*, thereby the positive charge was concealed inside the bacteria instead of being exposed to the surface [40,41]. Therefore, no effect on the potentials of *E. coli* was detected for smaller **TBC**. In contrast, **TBBC-C8** with C8 alkyl chains may be hindered by their interaction with bacteria due to larger steric hindrance [42,43], thus attenuating the bacteria imaging capability of **TBBC-C8**. Accordingly, zeta potentials results indicated that a significant impact of the size of the AIE PS molecules on the selective bacteria imaging.

Encouraged by the small ΔE_{ST} value of these BF_2-curcuminoids (**TBBC**, **TBC** and **TBBC-C8**), we further evaluated their $^1O_2$ generation ability in water under irradiation with green light ($\lambda = 530$ nm). The commercial 9,10-anthracenediyl-bis-(methylene)-dimalonic acid (ABDA) was utilized as an $^1O_2$ indicator to monitor the process of $^1O_2$ generation. As shown in Fig. 4a, upon irradiation with 530 nm green light (8.9 mW/cm^2), the absorbance intensity of ABDA gradually weakened in the presence of **TBBC** NPs, which is resulted from the decomposition by the increasing $^1O_2$ generation (Scheme S2 in Supporting information). As illustrated in Figs. S18 and S19 (Supporting information), the presence of the other two BF_2-curcuminoids NPs (**TBC** NPs and **TBBC-C8** NPs) also caused different degrees of decrease in the absorption intensity of ABDA, while that of ABDA alone changed slightly (Fig. S20 in Supporting information). Moreover, under the treatment of these BF_2-curcuminoids NPs (**TBBC** NPs, **TBC** NPs and **TBBC-C8** NPs), the higher decomposition rate of ABDA was detected compared with that of RB by monitoring the attenuation of absorption at 378 nm (Fig. 4b and Fig. S21 in Supporting information), indicating the superior $^1O_2$ generation performance of these BF_2-curcuminoids under 530 nm green light irradiation. In addition, the absorbance of ABDA was decreased by 57.0% in the presence of **TBBC** NPs upon irradiation with 530 nm green light for 80 s, suggesting that 7.13 μmol of ABDA was consumed per 20 s when 5 μmol/L of **TBBC** NPs was exposed to 530 nm green light. In contrast, 1.07 μmol and 4.45 μmol of ABDA were depleted per 20 s for 5 μmol/L of **TBC** NPs and **TBBC-C8** NPs under the same irradiation conditions, respectively. It was demonstrated that the $^1O_2$ generation efficiency of **TBBC** NPs was superior to that of **TBC** NPs, which is mainly attributed to the smaller ΔE_{ST} value for **TBBC** compared with **TBC**. Unexpectedly, $^1O_2$ generation per-

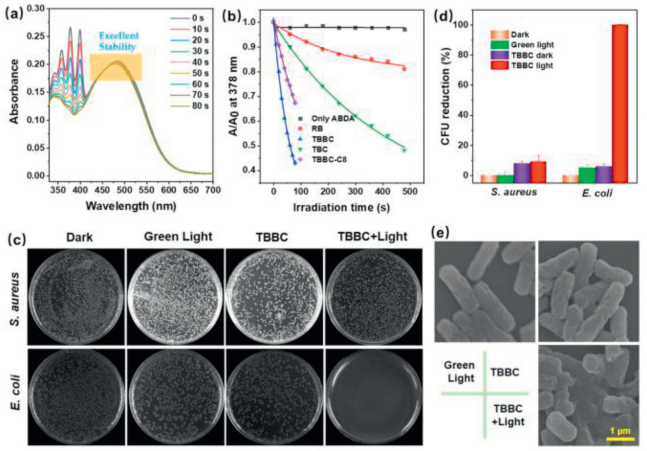

Fig. 4. The absorption spectra of ABDA in the presence of **TBBC** NPs under 530 nm green light irradiation (a). The decomposition rates of ABDA in the absence and presence of **RB**, **TBBC** NPs and **TBC** NPs under 530 nm green light irradiation (b), where A_0 and A are the absorbance of ABDA at 378 nm, [**RB**] = [**TBBC** NPs] = [**TBC** NPs] = [**TBBC-C8** NPs] = 5×10^{-6} mol/L, [ABDA] = 5×10^{-5} mol/L. Photographs of the agar plates (c) and CFU reduction (d) of *S. aureus* and *E. coli* with/without **TBBC** NPs (2×10^{-6} mol/L) and green light (8.9 mW/cm^2) treatment (e). Error bars: mean ± SD ($n = 3$). The SEM images of *E. coli* treated with or without **TBBC** NPs (2×10^{-6} mol/L) and green light irradiation (8.9 mW/cm^2).

formance for **TBBC-C8** with a smaller ΔE_{ST} was inferior to **TBBC** probably due to the influence of the hydrophobic C8 alkyl chains. Subsequently, the $^1O_2$ quantum yields of these BF_2-curcuminoids (**TBBC**, **TBC** and **TBBC-C8**) NPs in water were determined as 19%, 6%, 11% by using RB as the standard reference [44], respectively. Besides, it was noteworthy that **TBBC** NPs and **TBC** NPs displayed an excellent photostability in comparison with the commercial PS (RB) when exposed to green light probably because they were not easily oxidized by $^1O_2$, as depicted in Fig. 4a and Figs. S18 and S21, whereas **TBBC-C8** NPs showed a relatively poor photostability (Fig. S19), which may be attributed to the perturbation of the flexible C8 alkyl chains on the nanoparticles under green-light irradiation.

Inspired by the outstanding performance of $^1O_2$ generation and bacterial discrimination of the presented BF_2-curcuminoids, we further evaluated their photodynamic antibacterial activity by the classical plate colony-counting method [45,46]. Gram-positive *S. aureus* and Gram-negative *E. coli* were utilized as representative bacteria to probe their *in vitro* photodynamic antimicrobial properties under green light (8.9 mW/cm^2) irradiation, respectively. From Fig. 4c, both *S. aureus* and *E. coli* grew and reproduced smoothly on the agar plates in dark or green-light irradiation conditions when not treated with **TBBC** NPs. When both bacterial strains were treated with **TBBC** NPs and then stored in the dark, the colony-forming unit (CFU) of *S. aureus* and *E. coli* decreased by approximately 8% and 6% (Fig. 4d), respectively, implying its inconspicuous dark toxicity toward *S. aureus* and *E. coli*. In the presence of both **TBBC** NPs (2.0 μmol/L) and green light irradiation, *E. coli* was killed effectively with a nearly 100% CFU reduction rate of (Figs. 4c and d), while the photodynamic antimicrobial effect on *S. aureus* was negligible, and only *ca.* 9% CFU reduction rate was detected in comparison with the control groups. The photodynamic antimicrobial results thus indicated that **TBBC** NPs can eliminate selectively *E. coli* over *S. aureus via* antibacterial PDT. Subsequently, photodynamic antibacterial effects of **TBBC** NPs have been tested at two lower concentrations (*i.e.*, 1.0, 0.5 μmol/L). As shown in Fig. S22 (Supporting information), under the treatment of green light irradiation, about 60% of *E. coli* were killed at the concentration of 1.0 μmol/L, and almost 100% of *E. coli* survived when the concentration of **TBBC** NPs was decreased 0.5 μmol/L. Whereafter, scanning electron microscopy (SEM) was further employed to explore the detailed morphological changes of *E. coli* upon treatment with **TBBC** NPs and green light irradiation. As illustrated in Fig. 4e, the morphology of *E. coli* remained intact with smooth bodies when treated with only green light, while the treatment with **TBBC** NPs made the originally smooth bodies of *E. coli* become partially wrinkled probably owing to strong electrostatic interactions between **TBBC** NPs and *E. coli*. After *E. coli* was treated with both **TBBC** NPs and green light, the bacterial shape changed dramatically along with the fusion and shrinkage of cell walls, which definitely provided evidence that $^1O_2$ generated by **TBBC** NPs exerted toxicity to *E. coli*. These SEM results also revealed that the destruction of bacterial cell might be the main cause of the death of *E. coli*. By comparison, **TBC** NPs showed only almost 90% bactericidal rate against *E. coli* and an unconspicuous antimicrobial effect on *S. aureus* (Fig. S23 in Supporting information), suggesting a similar selective photodynamic antimicrobial activity to **TBBC** NPs. However, **TBBC-C8** NPs with four C8 alkyl chains hardly presented any photodynamic antimicrobial activity against *E. coli* and *S. aureus* (Fig. S24 in Supporting information). According to the previous reports [47–49], for **TBBC**, **TBC** and **TBBC-C8**, reasons for the discrepancy in photodynamic antimicrobial activity against *E. coli* may be attributed to the difference in molecular size of these AIE PSs. As was mentioned above, the poring channels in the outer envelope of Gram-negative bacteria (*E. coli*) can expel small dye molecules. Therefore, for the smaller-size **TBC** which showed partial photodynamic antimicrobial activity against *E. coli*, some of the PS molecules (**TBC**) may be pumped by the poring channels in the outer envelope of *E. coli* after exerting the photodynamic antibacterial effect to some extent, thus resulting in *ca.* 90% bactericidal rate against *E. coli*. As for C8 alkyl chains-functionalized **TBBC-C8**, the outer envelope of *E. coli* may not be crossed due to its larger size, leading to almost no photodynamic antimicrobial activity against *E. coli*.

To summarize, we successfully prepared three D-π-A-π-D type AIE photosensitizers (**TBBC**, **TBC** and **TBBC-C8**) based on BF_2-curcuminoid with yields ranging from 36% to 57%. These molecules incorporated substituted TPE groups as electron donors and AIE active moieties, BF_2bdk group as an electron acceptor, and a styrene (or ethylene) group as a π-bridge. Initial assessment of their photophysical properties revealed solvent-dependent behavior with large molar extinction coefficients in solvents of varying polarity and excellent AIE properties in mixed solvents, indicating that the inclusion of curcuminoid-BF_2 moieties did not compromise their AIE performance. Following this, the hydrophobic BF_2-curcuminoids were assembled into water-soluble nanoparticles (**TBBC** NPs, **TBC** NPs, and **TBBC-C8** NPs) with average hydrodynamic diameters ranging from 83 nm to 122 nm, emitting bright red fluorescence (640–668 nm) under 365 nm UV light. Surprisingly, bacterial staining experiments revealed that **TBBC** NPs selectively imaged Gram-negative *E. coli*, while no fluorescence signals were detected for **TBC** NPs and **TBBC-C8** NPs in either *S. aureus* or *E. coli*. Zeta potential (ζ) results indicated a significant impact of the AIE PS molecule size on selective bacteria imaging. Moreover, **TBBC** demonstrated efficient singlet oxygen generation when exposed to green light at 530 nm (8.9 mW/cm^2), attributed to its smaller singlet-triplet energy gap (ΔE_{ST}). Notably, it was noteworthy that **TBBC** NPs and **TBC** NPs displayed an excellent photostability compared with the RB under green-light irradiation, whereas **TBBC-C8** NPs showed a relatively poor photostability. More importantly, **TBBC** showed effective *in vitro* selective photodynamic killing of *E. coli*, likely due to its appropriate molecular size compared to **TBC** and **TBBC-C8**. In brief, **TBBC** holds great potential as a novel green light-excited AIE photosensitizer for discriminating and selectively sterilizing Gram-positive and Gram-negative bacteria.

Declaration of competing interest

The authors declare that they have no known competing financial interests or personal relationships that could have appeared to influence the work reported in this paper.

CRediT authorship contribution statement

Ziyong Li: Writing – review & editing, Writing – original draft, Funding acquisition, Formal analysis, Data curation. **Jinzhao Song:** Data curation. **Xinyu Gao:** Data curation. **Xiaoxie Ma:** Formal analysis, Data curation. **Keyu Liu:** Data curation. **Ziwei Ma:** Data curation. **Qilian Wang:** Data curation. **Xinliang Zeng:** Data curation. **Haining Zhang:** Data curation. **Pei Zhang:** Data curation. **Hui Guo:** Writing – review & editing, Writing – original draft, Supervision. **Jun Yin:** Writing – review & editing, Writing – original draft, Supervision.

Acknowledgments

The authors acknowledge financial support from National Natural Science Foundation of China (No. 32101150), Key Scientific Research Project of Higher Education of Henan Province (No. 22A430007), Natural Science Foundation of Henan Province (No. 222300420501), the Science and Technology Project of Henan Province (No. 242102230119), and Innovation and Entrepreneurship Training Program for College students in China (No. 202310482001).

Supplementary materials

Supplementary material associated with this article can be found, in the online version, at doi:10.1016/j.cclet.2024.110073.

References

[1] E. Svoboda, Nature 586 (2020) S58.
[2] X. Li, H. Bai, Y. Yang, et al., Adv. Mater. 31 (2019) 1805092.
[3] J.A. Bartell, L.M. Sommer, J.A. Haagensen, et al., Nat. Commun. 10 (2019) 629.
[4] E.D. Brown, G.D. Wright, Nature 529 (2016) 336–343.
[5] S.B. Levy, B. Marshall, Nat. Med. 10 (2004) S122–S129.
[6] A. Luther, M. Urfer, M. Zahn, et al., Nature 576 (2019) 452–458.
[7] J. Zhao, W. Wu, J. Sun, S. Guo, Chem. Soc. Rev. 42 (2013) 5323–5351.
[8] S.S. Lucky, K.C. Soo, Y. Zhang, Chem. Rev. 115 (2015) 1990–2042.
[9] X. Zhao, J. Liu, J. Fan, et al., Chem. Soc. Rev. 50 (2021) 4185–4219.
[10] X. He, L.H. Xiong, Z. Zhao, et al., Theranostics 9 (2019) 3223.
[11] D. Wang, M.M.S. Lee, W. Xu, et al., Theranostics 8 (2018) 4925.
[12] Z. Li, S. Chen, Y. Huang, et al., Chem. Eng. J. 450 (2022) 138087.
[13] B. Xue, X. Geng, H. Cui, et al., Chin. Chem. Lett. 34 (2023) 108140.
[14] Y. Jiang, Z. Zeng, J. Yao, et al., Chin. Chem. Lett. 34 (2023) 107966.
[15] L. Huang, D. Qing, S. Zhao, et al., Chem. Eng. J. 430 (2022) 132638.
[16] P.Z. Chen, L.Y. Niu, Y.Z. Chen, Q.Z. Yang, Coord. Chem. Rev. 350 (2017) 196–216.
[17] X. Zeng, X. Ma, J. Dong, et al., Angew. Chem. 135 (2023) e202312618.
[18] P. Zhang, Z.Q. Guo, C.X. Yan, W.-H. Zhu, Chin. Chem. Lett. 28 (2017) 1952–1956.
[19] S. Shen, W. Xu, J. Lu, et al., Chin. Chem. Lett. 35 (2024) 108360.
[20] X. Liu, Adv. Agrochem 2 (2023) 1–2.
[21] Z. Li, S. Hou, H. Zhang, Q, et al., Adv. Agrochem 2 (2023) 79–87.
[22] D. Li, T. Shen, X. Xue, et al., Sci. Chin. Chem. 66 (2023) 2329–2338.
[23] X. Ma, Y. Huang, W. Chen, et al., Angew. Chem. Int. Ed. 62 (2023) e202216109.
[24] S. Zeng, X. Liu, Y.S. Kafuti, et al., Chem. Soc. Rev. 52 (2023) 5607–5651.
[25] X. Ma, Y. Huang, A. Li, et al., ChemMedChem 18 (2023) e202300204.
[26] J. Zhang, C. Yue, Y. Ke, H. Qu, L. Zeng, Adv. Agrochem 2 (2023) 127–141.
[27] Y. Liao, Y. Liang, Y. Huang, et al., Chin. Chem. Lett. 35 (2024) 109092.
[28] X. Zeng, Y. Huang, J. Dong, et al., Yang, Adv. Agrochem 1 (2022) 73–84.
[29] Z. Li, X.-G. Yang, H. Zhang, et al., Inorg. Chem. Front. 9 (2022) 4281–4287.
[30] Z. Li, J.-R. Zhang, X.-K. Tian, et al., Chem. Sci. 13 (2022) 9381–9386.
[31] D.-H. Kim, A. D'aléo, X.-K. Chen, et al., Nat. Photonics 12 (2018) 98–104.
[32] H. Ye, D.H. Kim, X. Chen, et al., Chem. Mater. 30 (2018) 6702–6710.
[33] S. Xu, W. Wu, X. Cai, et al., Chem. Commun. 53 (2017) 8727–8730.
[34] X. Ding, Q. Wang, D. Chen, et al., Adv. Agrochem 2 (2023) 364–370.
[35] Z. Zhang, M. Kang, H. Tan, et al., Chem. Soc. Rev. 51 (2022) 1983–2030.
[36] Z. Li, X. Zeng, C. Gao, et al., Coord. Chem. Rev. 497 (2023) 215451.
[37] H. Zhang, C. He, L. Shen, et al., Chin. Chem. Lett. 34 (2023) 108160.
[38] Z. Li, X. Gao, H. Zhang, et al., Chin. Chem. Lett. 34 (2023) 107645.
[39] Y. Huang, W. Chen, J. Chung, et al., Chem. Soc. Rev. 50 (2021) 7725–7744.
[40] H. Yuan, Z. Liu, L. Liu, et al., Adv. Mater. 26 (2014) 4333–4338.
[41] H. Bai, H. Yuan, C. Nie, et al., Angew. Chem. Int. Ed. 54 (2015) 13208–13213.
[42] Y. Wang, T.S. Corbitt, S.D. Jett, et al., Langmuir 28 (2012) 65–70.
[43] H. Cai, X. Wu, L. Jiang, et al., Chin. Chem. Lett. 35 (2024) 108946.
[44] J. Ge, M. Lan, B. Zhou, et al., Nat. Commun. 5 (2014) 4596.
[45] A. Kaprelyants, D. Kell, J. Appl. Bacteriol. 72 (1992) 410–422.
[46] M. Dong, R. Tang, J. Li, et al., Chin. Chem. Lett. 35 (2024) 108539.
[47] K.R. Raghupathi, R.T. Koodali, A.C. Manna, Langmuir 27 (2011) 4020–4028.
[48] F. Perreault, A.F. De Faria, S. Nejati, M. Elimelech, ACS Nano 9 (2015) 7226–7236.
[49] L. Zheng, J. Li, M. Yu, et al., J. Am. Chem. Soc. 142 (2020) 20257–20269.